



# Applying In-Situ Radiography to Study Porosity Formation in Aluminum Welds

Real-time radiography was used to examine large gas pore movement in aluminum alloy weld pools

BY A. M. BARRAZA, C. E. CROSS, C. FINK, C. J. STULL, AND J. N. MARTINEZ

## Abstract

In-situ radiographic aluminum welding experiments were set up to observe the porosity formation and movement in aluminum weld pools. Aluminum Alloys 1100, 4047, and 6061 were autogenously gas tungsten arc welded while digitally recording radiograph images of macropores. Hydrogen was added in controlled parts per million through an argon-hydrogen shielding gas. The shielding gas hydrogen varied between 0 and 1000 parts per million of hydrogen, and three travel speeds were tested: 1.69, 2.54, and 3.39 mm/s. The transfer of hydrogen from the arc plasma to the weld pool was characterized using postweld gravimetric measurements to get the total pore volume and calculate weld metal hydrogen content. The amount of hydrogen added through the shielding gas played an important role in macropore volume and growth rate. Welding travel speed likewise played a critical role in hydrogen pickup. Alloy 1100 macropores originated at the bottom of the weld pool and then migrated upward toward the rear of the pool. Macropores in Alloys 4047 and 6061 originated at the leading edge of the weld pool and then moved downward and toward the rear of the pool. It is hypothesized that this difference in behavior is related to Marangoni-controlled fluid flow in Alloys 4047 and 6061.

## Keywords

- Aluminum
- Hydrogen
- Porosity
- Radiography
- In-Situ

## Introduction

While porosity in aluminum welds continues to be a difficult problem for industry, there has been little research performed to understand where it originates and how it moves and grows within the weld pool. Weld porosity, found in many different metal alloy systems, is normally related to a drop in solubility of interstitial elements during solidification. Pores can also form from keyhole and arc instabilities, but the partial pressure of dissolved interstitials is still involved. Porosity in aluminum is specifically associated with hydrogen contamination (Ref. 1), but how and where it nucleates, moves, and grows has been left to speculation.

Most structural aluminum welds are evaluated according to specifications that limit the amount and/or size of pores that can be tolerated. Uniformly distributed porosity itself does not necessarily lower mechanical properties, aside from reducing the load-bearing area (Ref. 2). But at high volume levels or for closely spaced linear porosity, problems with crack initiation, propagation, and leak tightness may be encountered, particularly under fatigue loading. Postweld radiography and cross-sectional metallography are common tools used to characterize weld porosity. However, these techniques do not show the origin of pores and indicate only the location where pores were overgrown (i.e., engulfed) by the advancing solid/liquid interface. Additionally, there

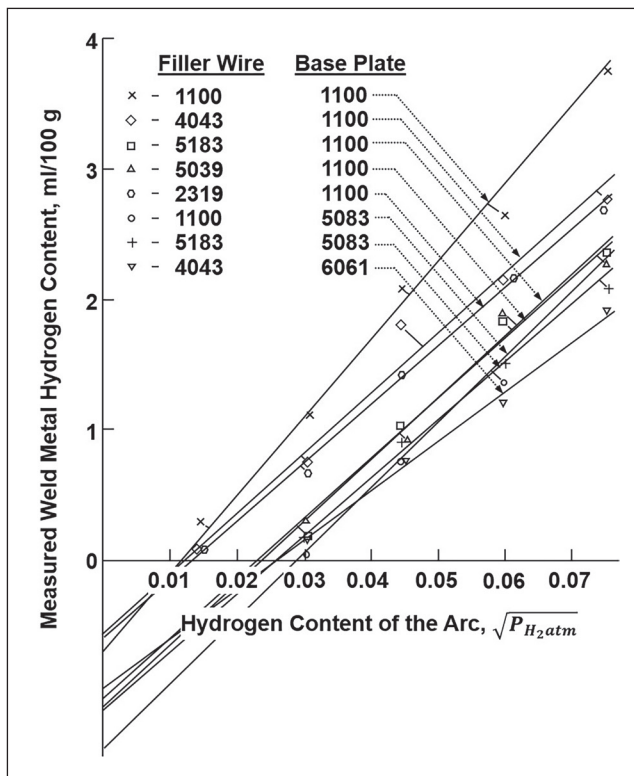


Fig. 1 — Data from the work of Woods (Ref. 6) showing amount of weld metal hydrogen, based upon gravimetric analysis, as a function of hydrogen partial pressure in the shielding gas. Shown is data for different aluminum base plates and filler alloys.

is no indication of the number of pores that escaped during welding.

This in-situ study is unique in that it used real-time radiography to examine porosity caused by controlled additions of hydrogen to the argon shielding gas. The thin section coupons used here (3 mm [0.118 in.] thick) were edge welded using autogenous gas tungsten arc welding (GTAW) that allowed for better resolution of pores when viewed normal to the weld. Micropores (e.g., interdendritic pores, < 10 μm diameter) could not be easily resolved, but macropores (> 10 μm) were observed and their behavior in the weld pool was documented and quantified. Three different aluminum alloys were studied (1100, 4047, and 6061), which gave insight into distinctive macropore shapes, growth behavior, and migratory patterns.

Gravimetric analysis performed on the weld metal from each welded coupon gave the amount of absorbed hydrogen in each case, based upon volume-percent (vol-%) porosity. This data allowed for a comparison of the effects of weld travel speed and parts per million (ppm) of shielding gas hydrogen for each alloy welded. Metallographic cross sections were used to verify radiographic analysis.

## Background

### Hydrogen Solubility

Hydrogen contamination can come from many sources, including shielding gas moisture, hydrated surface oxides on wire and weld joints, and hydrogen dissolved in the base metal and filler wires (Ref. 3). Little knowledge is available regarding how effectively hydrogen can be transferred from the arc plasma to the weld pool or how much hydrogen can be tolerated in the weld pool before porosity is nucleated. It is clear, however, that aluminum weld metal exhibits a much higher solubility than equilibrium predictions made using Sievert's Law (Ref. 4):

$$[H] = K\sqrt{p_{H_2}}, \text{ where } \log K = \left[ \frac{-2760}{T} + 2.796 \right] \quad (1)$$

with the partial pressure of hydrogen  $p_{H_2}$  in standard atmosphere (atm), the temperature  $T$  in Kelvin, and hydrogen concentration  $[H]$  in ml/100 g. Assuming the weld pool is superheated to approximately 800°C, as commonly observed in aluminum welds (Ref. 5), Equation 1 predicts a solubility of 0.053 ml/100 g at a partial pressure of 0.001 atm (1000 ppm). This solubility is significantly lower than the measured values of 1–2 ml/100 g for much lower partial pressures (Ref. 6). This large deviation from equilibrium has also been observed in ferrous systems regarding hydrogen and nitrogen pickup (Ref. 7). This is believed to be associated with the monatomic form of interstitial hydrogen prevalent in the arc plasma, as opposed to the diatomic form assumed in Sievert's Law (Ref. 7). High weld pool surface temperatures, approaching the vaporization temperature, may also account for higher solubility. High concentrations of dissolved hydrogen at the pool surface, related to this high temperature, could then become mixed into the bulk liquid through convection.

Additional factors, such as weld parameters that influence arc and weld pool size (Ref. 6), can affect hydrogen pickup in the weld pool. The large pool surface area allows more hydrogen to enter (or escape) the weld pool. Arc-pool exposure time, determined by the weld travel speed, also affects this. The travel speed also limits the time for pore nucleation, growth, and escape. Buoyancy forces act to cause some pores to migrate against gravity and escape, depending upon the orientation of welding. Some porosity evaluation tests require that welds be made overhead to avoid escape. Material composition may also have a large effect (Ref. 7).

### Origin of Pores

Porosity formation can be influenced by solidification and can reasonably be assumed to originate first between dendrites since this is where hydrogen is concentrated during solidification due to the partitioning of interstitial atoms (Ref. 8). It has been suggested that interdendritic micropores (< 10 μm diameter) may be washed ahead of the solidification

**Table 1 — Nominal and Measured Aluminum Alloy Compositions**

Alloy Type	Composition in Weight Percent (wt-%)*							
	Si	Fe	Cu	Mn	Zn	Ti	Mg	Al
<b>1100-H14</b> (ASTM B209-14)	0.13 (0.95 Si + Fe)	0.6	0.12 (0.05–0.2)	0.01 (0.05)	< 0.01 (0.1)	< 0.001 (–)	< 0.001 (–)	Bal. (99.0 minimum)
<b>4047-F</b> (Similar to AWS A5.8)	11.6 (11.0–13.0)	0.3 (0.8)	0.03 (0.30)	0.06 (0.15)	0.12 (0.20)	0.02 (–)	0.08 (0.10)	Bal.
<b>6061-T6</b> (ASTM B209-14)	(0.4–0.8)	(0.7)	(0.15– 0.40)	(0.15)	(0.25)	(0.15)	(0.8–1.2)	Bal. (99.0 minimum)

\*Specification limits in brackets are given as wt-% maximum unless otherwise stated.

front, where they grow and coalesce (Ref. 9). The partition coefficient for hydrogen in pure aluminum is small ( $k = [H_s] / [H_l] = 0.05$  [Ref. 1]), which represents a significant drop in solubility during solidification.

For pores to nucleate, sufficient hydrogen supersaturation is required to overcome surface tension and external pressure. Nucleation is most likely to occur on existing substrates, such as dendrites, second phase particles, or oxides. Internal pressures on the order of 1760 atm have been proposed for heterogeneous nucleation (Ref. 10). The interdendritic pressure drop associated with solidification aids in achieving this condition. Based upon this criterion, a calculated weld pool hydrogen concentration of 1.6 ml/100 g is needed to nucleate micropores at the base of dendrites in Aluminum Alloy 6060 (Ref. 9).

### Threshold Hydrogen Levels

Woods (Ref. 6) demonstrated that hydrogen pickup in aluminum weld metal increases with hydrogen partial pressure and varies with alloy content — Fig. 1. This graph was plotted assuming a Sievert's relationship (Equation 1), which is now believed to be questionable for arc welds. He determined weld metal hydrogen content based upon a gravimetric method for gas volume determination. When solubility becomes zero, this signals that pores are present and thus indicates the contamination level needed for pore formation. Woods (Ref. 6) suggested that pores form when superheated and supercharged molten metal, located directly under the arc, is rapidly transferred to cooler regions of the pool, leading to supersaturation. It should be noted that Alloy 1100, with the lowest alloy content, had the greatest amount of hydrogen pickup during welding and the lowest threshold for pore formation.

**Table 2 — Gas Tungsten Arc Welding Parameters**

<b>AC balanced square wave</b>	75% EN, 25% EP
<b>Arc current</b>	50–80 A (root mean square)
<b>Arc voltage</b>	12 V
<b>Travel speed</b>	1.69, 2.54, and 3.39 mm/s
<b>Ceriated tungsten electrode</b>	2.38 mm diameter, 30-deg tip angle

### Movement, Engulfment, and Escape

It is reasonable to assume that pores cannot move freely within the bulk of the weld pool, where flow velocities of 0.1 m/s have been estimated (Ref. 11). Associated drag and shear forces would tear macropores apart. Hence, they most likely reside next to the solid/liquid interface in a diffuse boundary region where flow velocities tend to zero. What causes some



Fig. 2 — Photograph of experimental setup for digital radiography showing an aluminum plate specimen, GTAW torch, and stationary aligned x-ray source (red).

pores to become engulfed (i.e., overgrown) by the advancing solid/liquid interface must also be considered. If pores behave in a manner similar to oxide particles, there exists a critical velocity, depending upon pore size, above which the drag force promotes engulfment (Ref. 12). The larger the pore, the greater the drag force becomes and the lower the critical velocity needed for engulfment.

If not engulfed, it follows that the pores are pushed forward ahead of the melt pool boundary with the possibility that they grow and coalesce. Buoyancy also works on the pore to move it against gravity, which may involve movement to the pool surface and escape. This outgassing (i.e., effervescent bursting of pores at the pool surface) can be observed when welding material with high interstitial content. As will be shown in this study, the liquid flow pattern within the weld pool can also affect pore movement.

## In-Situ Radiography

Previous studies have used in-situ radiography to examine welding. In 1988, Dixon et al. (Ref. 13) were among the first to report this technique. Placing an x-ray source above a moving GTA weld on a thin 0.9-mm (0.035-in.) steel plate, prestressed to induce cracking, they observed porosity and solidification cracks. The study was done prior to the existence of digital cameras and utilized a video tape cassette camera to record images directly off a phosphorous intensifier screen. Rokhlin and Guu (Ref. 14) monitored weld defects and incomplete joint penetration in submerged arc welding using a similar method, which when combined with digital image analysis, provided information for adaptive feedback control. Recent studies have viewed keyhole formation in laser welds on stainless steel (Ref. 15) and aluminum

Table 3 — Controlled Shielding Gas Mixtures of Argon (Ar) and Ar-0.1% H<sub>2</sub>

Combined Shielding Gas Flow Rate = 30 ft <sup>3</sup> /h		Total H <sub>2</sub> (ppm)
Ar (ft <sup>3</sup> /h)	Ar + 0.1% H <sub>2</sub> (ft <sup>3</sup> /h)	
0	30	1000
5	25	833
10	20	667
15	15	500
20	10	333
25	5	167
30	0	0

(Ref. 16) and solidification crack growth in GTA aluminum welds (Ref. 17).

## Experiment

### Material

Autogenous, automatic GTA welds were made along the edge of 3-mm-thick specimens (76 mm [2.99 in.] height × 127 mm [5 in.] length) cut from a 3-mm rolled plate. Welds were made in the direction of rolling. Weld preparation consisted of abrading the weld edge with a scouring pad and wire brush followed by acetone cleaning to remove abraded oxidation and any residual oil. Three different aluminum alloys were examined (Alloys 1100-H14, 4047-F, and 6061-T6), representing a broad spectrum of weldability and anticipated pool behavior. The chemical composition of these alloys is listed in Table 1. Measured compositions for Alloys 1100-H14 and

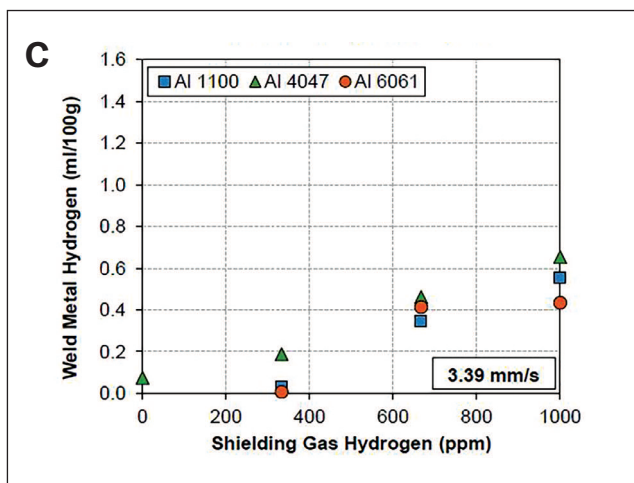
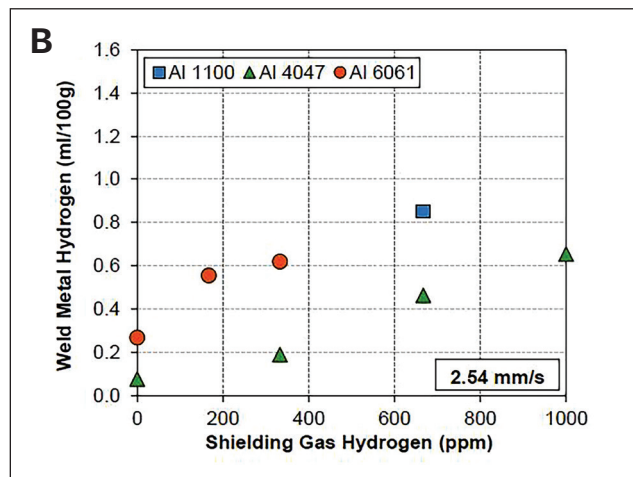
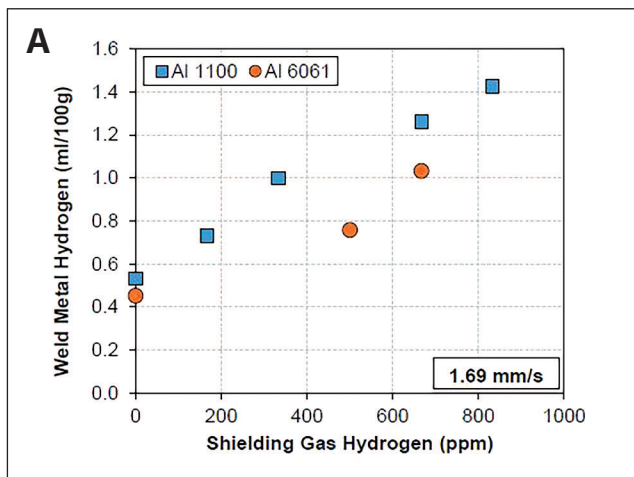


Fig. 3 – Weld metal hydrogen content as a function of hydrogen in shielding gas mixture, calculated based upon the gravimetric data. Shown is data for three weld travel speeds: A – 1.69; B – 2.54; C – 3.39 mm/s.

4047-F are based upon the manufacturer’s certificate of chemical analysis.

Alloy 1100 is unalloyed (99 wt-% commercial purity) and has a high melting point and narrow solidification range (657°–643°C) (Ref. 18). Alloy 4047 contains nominally 11–13 wt-% silicon. It is a near-eutectic composition useful for brazing and can be characterized as having exceptional pool fluidity, low melting point, and a narrow solidification range (582°–577°C) (Ref. 19). Alloy 6061 is a heat-treatable grade alloyed with magnesium (0.8–1.2 wt-%) and silicon (0.4–0.8 wt-%) to form  $\beta$ (Mg<sub>2</sub>Si) precipitates. This alloy has a large solidification range (652°–582°C) and tends to form a thick pool oxide, contributing to its pool sluggishness (Ref. 18).

## Welding Process

An alternating current (AC) power supply was chosen because of its controllable heat input and cleaning action. A 75% negative electrode (EN) and 25% positive electrode

(EP) balance control was selected to give the optimum welding result for this application. A ceriated tungsten electrode, 2.38 mm (0.0937 in.) diameter, was ground to a point. Due to the electrode positive portion of the cycle, the electrode tip was partially melted, as observed in radiographs.

Welding parameters are given in Table 2, where the welding current was adjusted to maintain a nominal weld pool depth of approximately 3 mm (0.118 in.) for the various travel speeds, hydrogen contents, and alloys examined. Weld travel speed was varied to identify kinetic effects on pore growth. Alloy 1100 required a higher current because of its higher thermal conductivity. Welds made with high hydrogen shielding gas required a reduced current due to the higher thermal conductivity of the hydrogen and hotter arc. Hydrogen addition to argon increases the voltage drop in the arc and increases the energy concentration (Ref. 20). For tests run at increased travel speed, an increase in current was needed to achieve the desired constant pool size. A full set of parameters for each welded sample can be found in Ref. 21.

The variable hydrogen content in the argon shielding gas mixture was achieved by mixing controlled amounts (i.e., flow rates) of 99.999% argon and premixed 99.999% argon + 1000 ppm of hydrogen. The total flow rate was kept constant at 850 L/h (30 ft<sup>3</sup>/h). The actual mixtures that were used are tabulated in Table 3, varying from 0 to 1000 ppm hydrogen. This span of hydrogen contamination was selected based upon preliminary work.

## Radiography

The entire weld pool was imaged during welding using digital radiography, transverse to the welding direction. Figure 2 shows a photograph of the experimental setup in the radiography chamber. The digital radiography equipment used in this study was a Hamamatsu 150 eV x-ray source with a North Star X25 industrial x-ray inspection system, normally used for 3D topographic analysis, coupled with a PaxScan® 2520DX digital x-ray flat panel detector. Frame rate and magnification were varied during initial development to achieve the optimum resolution. Radiographic operating parameters used are listed in Table 4.

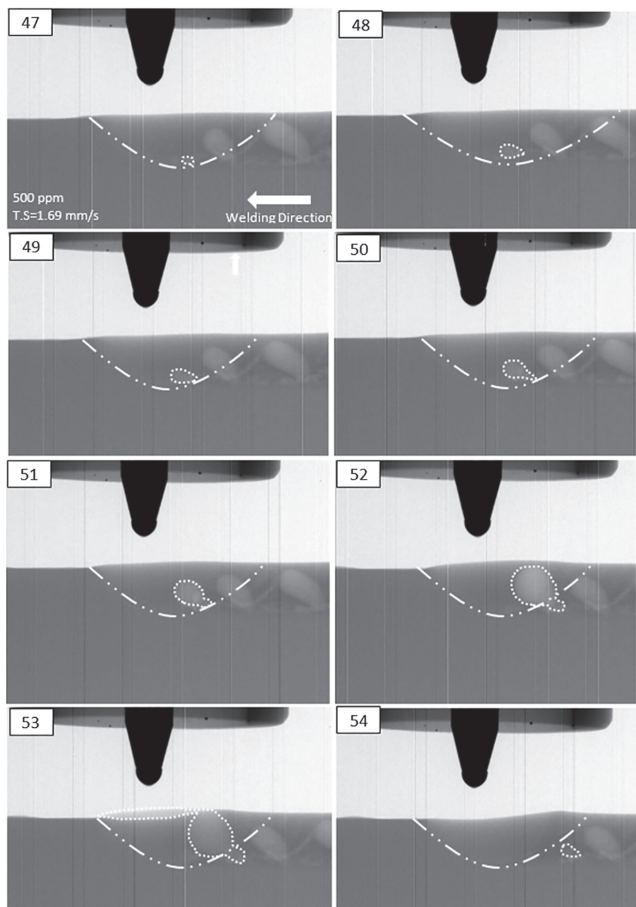


*Fig. 4 – Alloy 1100 weld radiograph series made with 500 ppm shielding gas hydrogen at a travel speed of 1.69 mm/s shows pore formation at the bottom of the weld pool and pore gas entrapment and escape. The same pore is being tracked from frame to frame. The time between frames is 133.3 ms.*

The aluminum test specimen was secured in a vise on a moving slide table. The GTAW torch was mounted to a stationary arm fixed to the floor of the experimental chamber. The motorized slide table traversed the secured aluminum plate underneath the stationary GTA torch at a fixed speed. The electrode-to-workpiece distance was maintained at 2.4 mm (0.094 in.) by leveling the welding edge of the aluminum plate in the vise. The x-ray source was positioned perpendicular to the plate to observe the weld pool during the welding process. This allowed direct viewing of where macropores formed and where they tended to migrate. In some cases, it allowed for pore growth to be measured.

## Video Processing

The raw data from the in-situ radiographs were digitally recorded. The radiographs, referenced from a fixed point forward as a series of frames, were processed to enhance the contrast and then cropped to bring the area of interest to center view. The frames were stacked together to create a movie and image stack (a time series of TIFF files). The TIFF stack was opened in an image processing software, ImageJ,

**Table 4 – Operating Parameters Used for Digital Radiography**

Energy (keV)	100
Current ( $\mu$ A)	100
Frame rate (fps)	7.5 and 30
Source-to-detector distance (mm)	381 and 762
Source-to-part distance (mm)	38.1 and 76.2
Magnification	10 $\times$
Binning	2
Effective pixel size ( $\mu$ m)	25.4

to take pixel measurements. The known electrode diameter measurement was taken using the image processing software, yielding the diameter measurement in pixels. Pores were tracked through frames, and their diameters were measured using ImageJ.

## Gravimetric Testing

The gravimetric test was conducted to determine the percent volumetric porosity in the weld metal samples and calculate the weld metal hydrogen content. The test was conducted in a temperature-controlled environment. The gravimetric specimens were extracted from the samples welded for radiography using a hand-operated shear and were approximately 44.4 mm (1.75 in.) long. Each specimen surface was thoroughly cleaned with ethanol to remove any residual oil, grease, and dust. Using an analytical balance, each specimen was weighed five times on a dry platform and then on a platform immersed in water. The immersed mass measurement was recorded once the water was free of visible air bubbles. The immersed mass and wet mass were measured five times for each specimen. The data was then

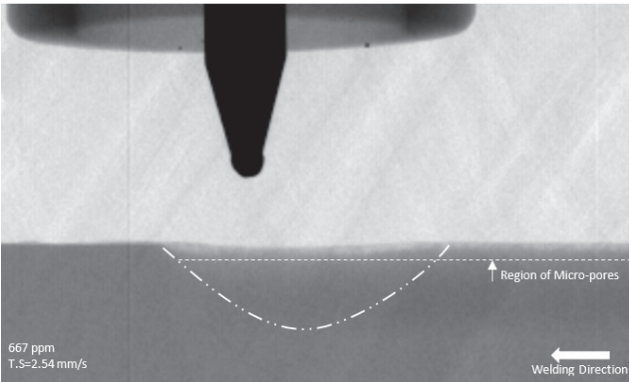


*Fig. 5 – Alloy 4047 weld radiograph frame made with 667 ppm shielding gas hydrogen at a travel speed of 2.54 mm/s shows microporosity at the leading and trailing edges of the weld pool.*

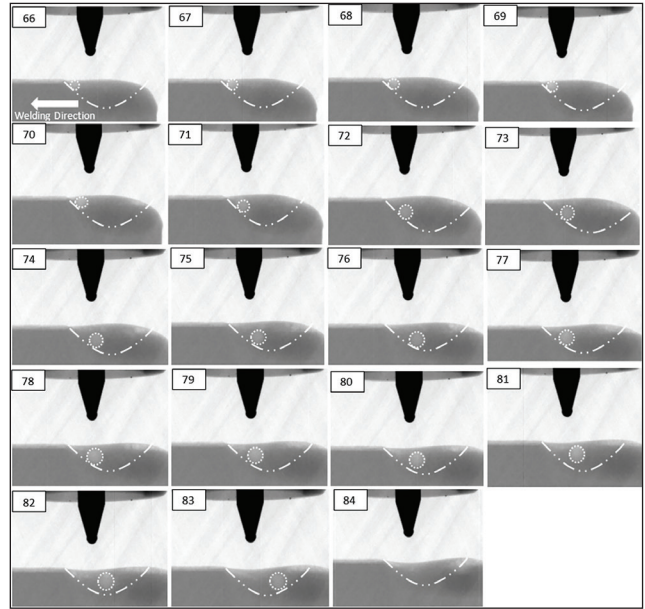


*Fig. 6 – Alloy 4047 weld radiograph series using 1000 ppm shielding gas hydrogen at a travel speed of 2.54 mm/s shows pore movement. The same pore is being tracked from frame to frame. The time between frames is 33.3 ms.*

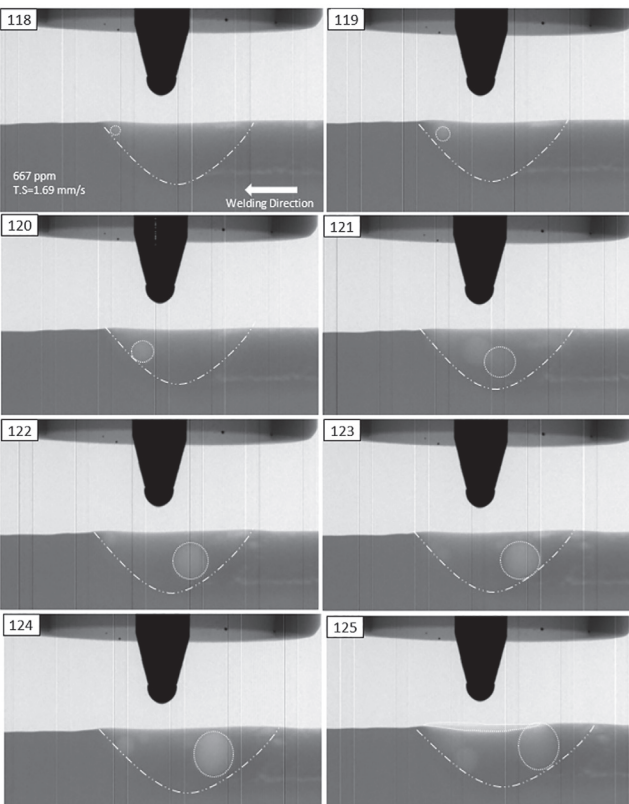


*Fig. 7 – Alloy 6061 weld radiograph series with 667 ppm shielding gas hydrogen at a travel speed of 1.69 mm/s shows pore escaping in the final frame. The same pore is being tracked from frame to frame. The time between frames is 133.3 ms.*

used to obtain the volume percent porosity. The weld metal hydrogen content was calculated by multiplying volume percent porosity by the volume of 100 g of alloy. This gave the volume of diatomic hydrogen in 100 g weld metal at standard temperature and pressure (STP).

## Results

### Hydrogen Transfer

As expected from Woods's work (Ref. 6; see Fig. 1), an increase in weld metal hydrogen content with increased additions of hydrogen to the shielding gas was observed, as shown in Fig. 3. The difference here is that the weld metal hydrogen content is plotted against partial pressure hydrogen, not the square root pressure since there is no reason to expect Sievert's Law to apply. It is interesting to note that for the slowest weld travel speed (1.69 mm/s), Alloy 1100 picked up the greatest amount of hydrogen from the arc, similar to Fig. 1. At the highest travel speed, there was less discernable difference between alloys. Also note that at increasing travel speed, the hydrogen pickup was significantly diminished. This may be because at higher travel speed, the time of the weld pool exposure to the arc is reduced.

### Pore Migration

Presented in this section are figures showing select radiograph frames found most representative of a particular alloy and welding condition. Data is presented through a series of frames (welding direction from right to left), with each frame numbered (top left-hand corner). Each frame shows an outline of the weld pool for orientation purposes. In some frames, a particular macropore is also outlined to indicate the pore is being tracked.

It was observed that the macropores originated either at the pool bottom (Alloy 1100) or at the pool front (Alloys 4047 and 6061). This supports Woods's hypothesis that pores

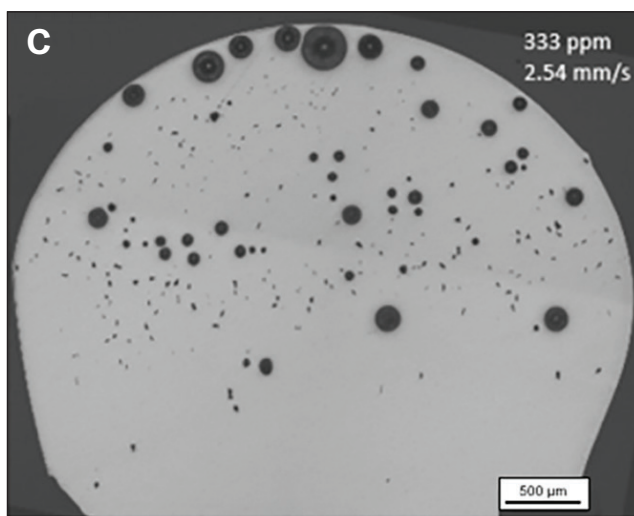
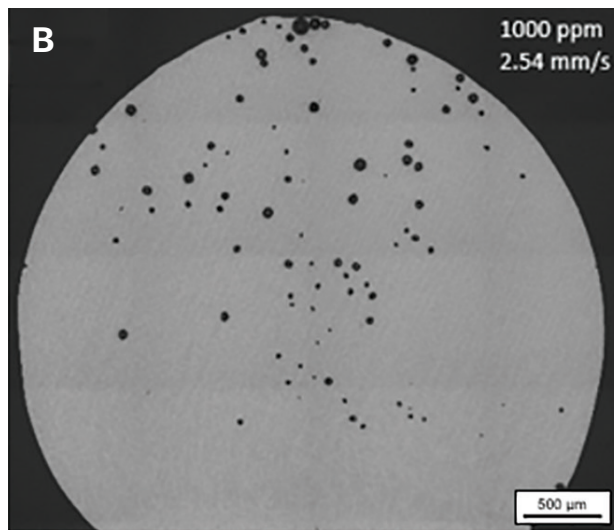
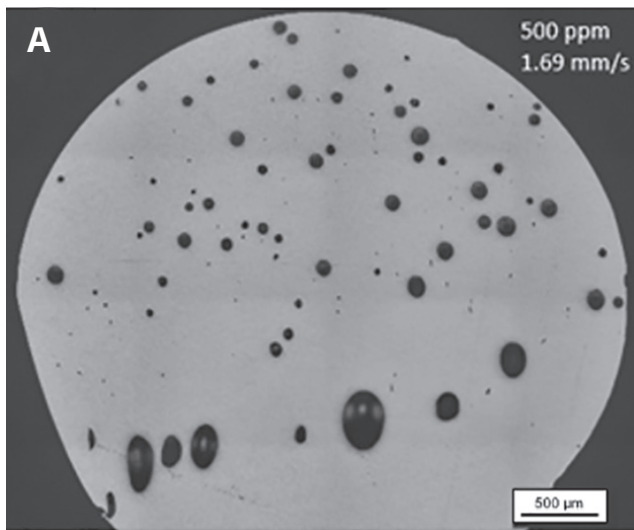


*Fig. 8 – Macrographs showing pore shape and location in transverse weld cross sections: A – Alloy 1100; B – Alloy 4047; C – Alloy 6061.*

nucleate within the weld pool due to the rapid cooling of supercharged liquid, moving from under the torch to the cooler pool periphery (Ref. 6). When macropores were first observed in this study, they were approximately 90 µm in diameter, and it was assumed they grew from a much smaller nucleus.

Figure 4 shows an Alloy 1100 sample welded with 500 ppm shielding gas hydrogen at a travel speed of 1.69 mm/s. The tracked pore is first observed in frame 47 as a micropore at the bottom edge of the weld pool. It is within 0.133 s, the time between frames, that the pore transformed into a measurable macropore. The trailing edge of the pore seemed to be pinned in the solidified region, causing the pore to grow in an elliptical shape. As the pore continued to accumulate hydrogen and grew, the shape became elongated, resulting in a light-bulb-shaped pore.

The rapid pore growth ended in frame 53, when the pore gas escaped at the surface, which can be seen as a halo over the weld pool. In frame 54, the void left behind from the pore

was quickly backfilled with molten metal, leaving behind a small cavity that had already been overgrown by the solidification front. The final pore size, as seen in frame 53, had a maximum diameter of approximately 2.0 mm (0.078 in.) and was approximately 2.6 mm (0.10 in.) in length. Due to its irregular shape, the average growth rate was not calculated. The time for this pore to grow and for gas to escape was approximately 0.93 s. It can also be seen throughout this set of frames that not every macropore breached the surface. The macropores to the right of the previously mentioned macropore had been completely engulfed by the solidified weld metal.

Figure 5 shows one representative frame from an Alloy 4047 sample welded with 667 ppm of hydrogen in the shielding gas at a travel speed of 2.54 mm/s. Micropores were observed, barely resolvable, on the weld pool surface, seen above the dashed line in Fig. 5. No macropores were resolvable within the weld pool. However, there were clear indications of micropores clustered at the leading and trailing edges of the weld pool surface. This behavior was observed throughout the Alloy 4047 welded samples beginning at shielding gas hydrogen levels of 333 ppm and greater. In Fig. 5, the entrapped micropores can be seen near the top edge of the weld. During the experiments with a slower travel speed of 2.54 mm/s, the areas of microporosity showed up as brighter clusters on the images, indicating a more densely populated area with micropores.

Figure 6 shows an Alloy 4047 sample welded with 1000 ppm of hydrogen in the shielding gas at a travel speed of 2.54 mm/s. This set of frames captured the only macropore observed in any Alloy 4047 welded sample. The macropore, shown in frame 66, formed at the leading edge of the weld pool and remained in the shape of a sphere during its growth period. The macropore stayed in the top region of the weld pool until it was swept downward and back toward the trailing edge of the weld pool. The macropore then floated upward toward the surface of the weld pool, where it eventually breached the surface, losing the trapped gas. The final pore size, as seen in frame 83, was 1.48 mm in diameter.

Figure 7 shows an Alloy 6061 sample welded with 667 ppm shielding gas hydrogen at a travel speed of 1.69 mm/s. Frame 118 shows a small macropore, spherical in shape, which

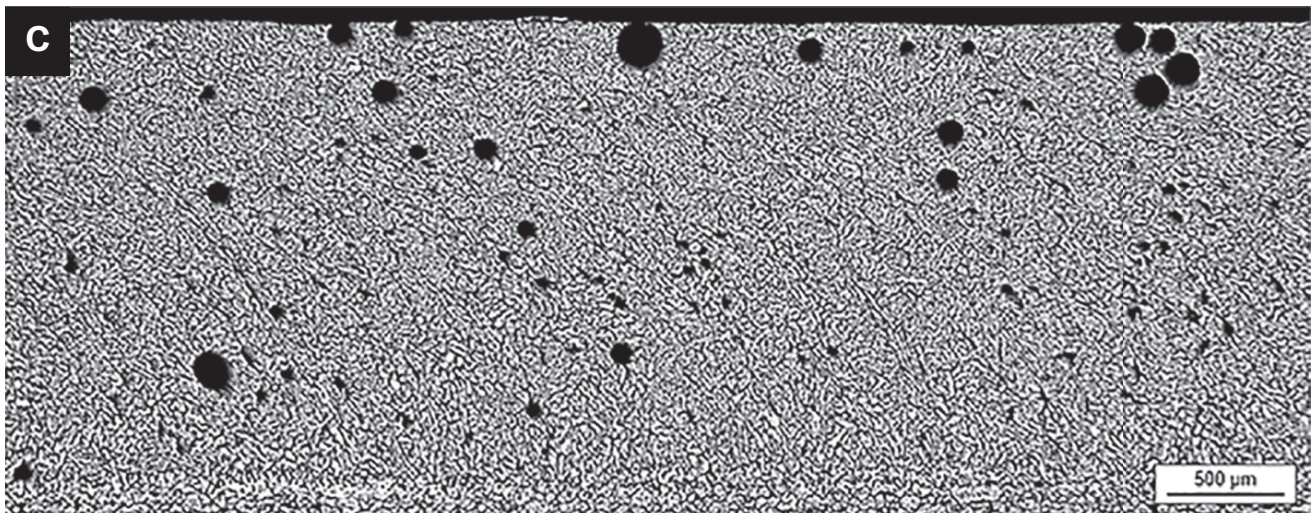
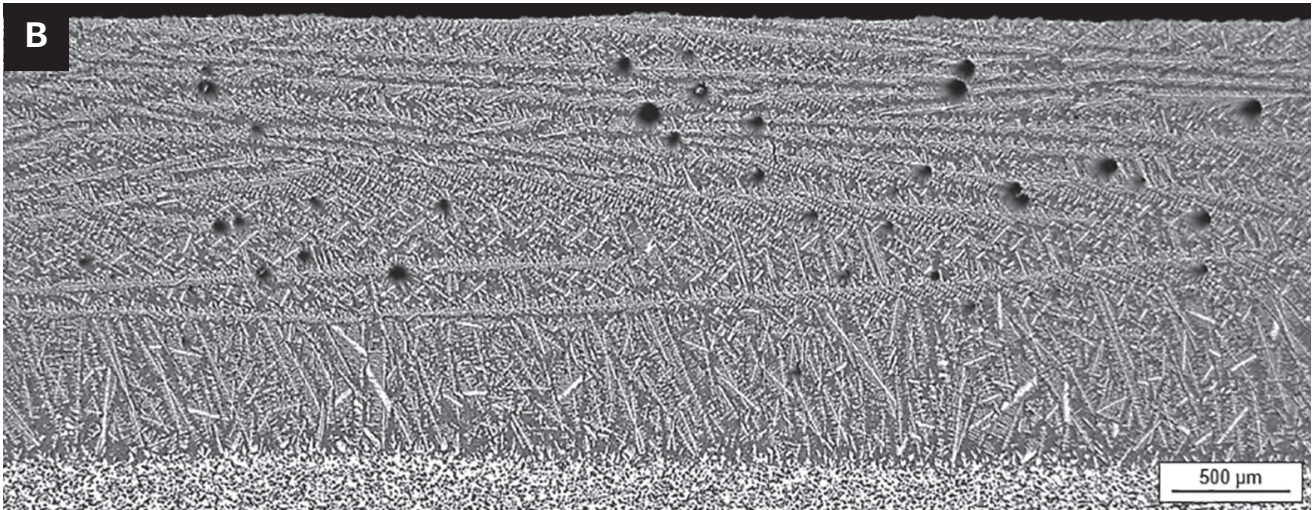
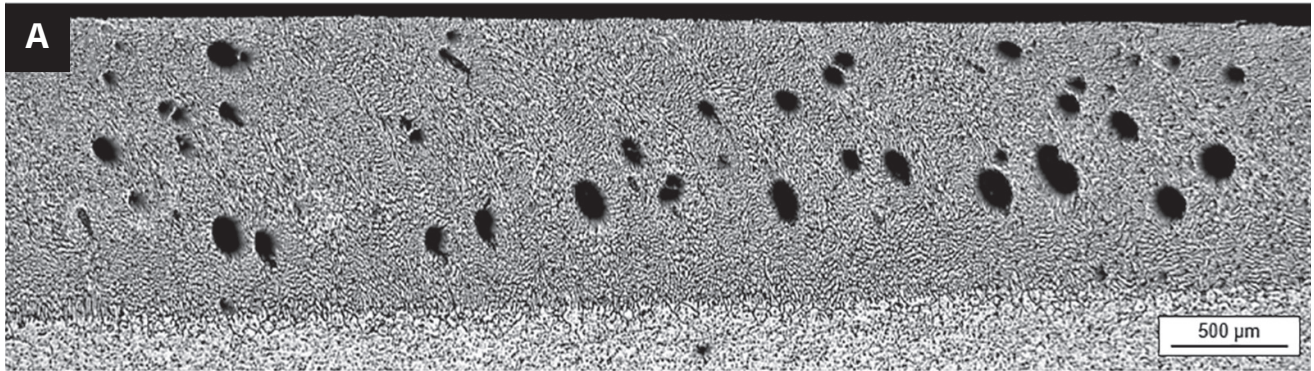


*Fig. 9 – Macrographs showing pore shape, size, and location for longitudinal weld cross sections: A – Alloy 1100; B – Alloy 4047; C – Alloy 6061. All welds were made at 667 ppm shielding gas hydrogen at a travel speed of 3.39 mm/s. The welding direction was from right to left.*

formed at the leading edge of the weld pool. Within a few milliseconds, the macropore was pushed to the bottom of the weld pool and then swept quickly upward to the trailing edge of the weld pool. In the final frame where the pore is observed, frame 125, the pore breached the weld pool surface, and the pore gas escaped and covered the weld pool

surface. The final pore size, as seen in frame 124, was 1.82 mm (0.07 in.) in diameter with an average surface area growth rate of 3.14 mm<sup>2</sup>/s as calculated from the cross-sectional pore radii. The time for this pore to grow was approximately 1.06 s from beginning to end.

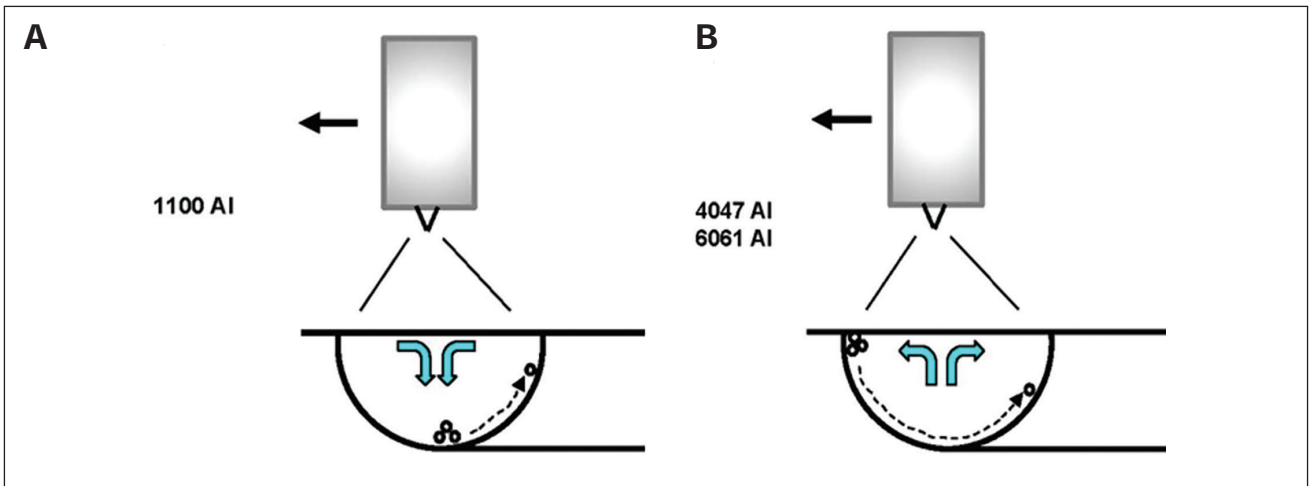


Fig. 10 — Schematic of the effect of different fluid flow patterns on pore migration in aluminum alloy welds: A — 1100; B — 4047 and 6061.

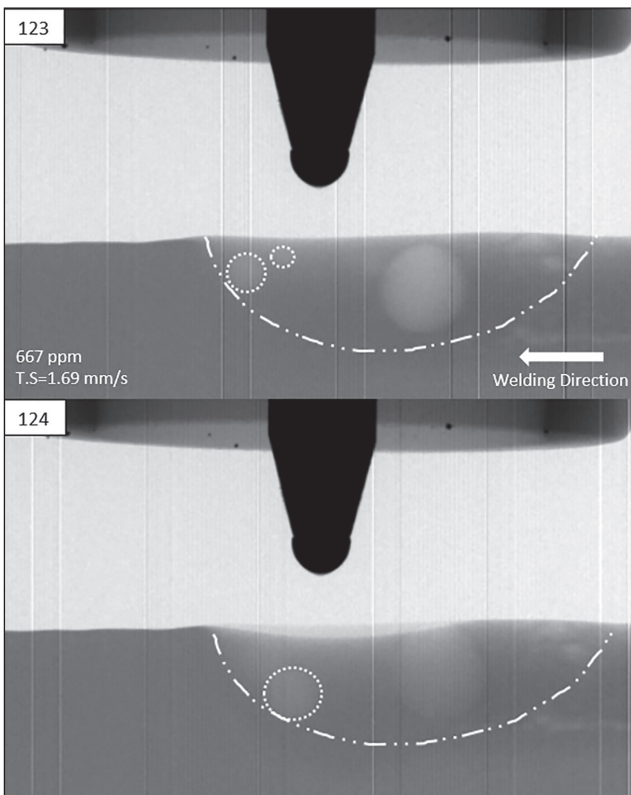


Fig. 11 — Example of pore coalescence in the Alloy 6061 weld made with 667 ppm shielding gas hydrogen at a travel speed of 1.69 mm/s. Two pores in frame 123 became one pore in frame 124.

## Pore Distribution

Macrographs prepared from transverse and longitudinal cross sections of the welds on each alloy tend to support observations from the in-situ data. They also show the presence of microporosity that could not be resolved with radiography. As described previously, the pores observed in these macrographs were engulfed by the advancing solid/

liquid interface. Not seen are the many pores that escaped before being engulfed. In Fig. 8, transverse cross sections of the three alloys are shown to highlight the difference in observed pore size and distribution. Figure 8A shows an Alloy 1100 weld made with 500 ppm of shielding gas hydrogen at a travel speed of 1.69 mm/s. The macropores are located mostly at the bottom of the weld. Figure 8B shows an Alloy 4047 weld made with 1000 ppm of shielding gas hydrogen at a travel speed of 2.54 mm/s. There is an absence of macropores, but micropores are found throughout the cross section, with clustering at the weld crown. Figure 8C shows an Alloy 6061 weld made with 333 ppm of shielding gas hydrogen at a travel speed of 2.54 mm/s. A mixture of macro- and micropores can be seen with the larger macropores near the crown of the weld.

Longitudinal weld cross sections for the three alloys are compared in Fig. 9. All welds were made at 667 ppm shielding gas hydrogen at a travel speed of 3.39 mm/s. Figure 9A shows an Alloy 1100 weld with numerous large macropores just below the midpoint of the weld. These pores are unique in that they are elongated. Very few micropores are found. Figure 9B shows an Alloy 4047 weld without any macropores, but numerous micropores are dispersed in the upper half of the weld. Figure 9C shows an Alloy 6061 weld made with micropores distributed throughout and spherical macropores primarily located in the upper half of the weld.

## Discussion

### Pore Migration

It is clear from the different pore movement in the Alloy 1100 vs. the Alloys 4047 and 6061 welds that these pores were influenced by fluid flow patterns characteristic of these alloys. Such differences in behavior could be described by the schematics shown in Fig. 10. In the case of Alloy 1100, hot liquid under the arc was transferred to the bottom of the pool, whereas in the case of Alloys 4047 and 6061, liquid was transferred to the pool periphery. Such differences in

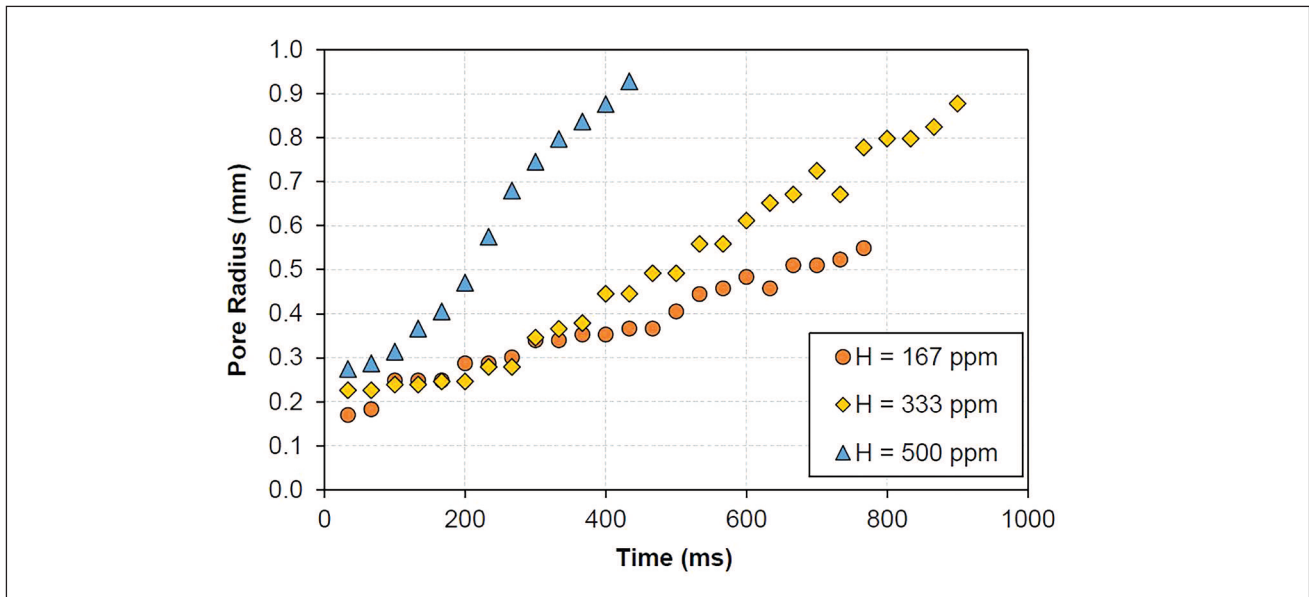


Fig. 12 — Individual pore radii measured over time for different hydrogen shielding gas additions. Data shown for Alloy 6061 welded at 2.54 mm/s travel speed.

behavior could be caused by Marangoni flow, driven by the relationship between surface tension and temperature (Ref. 22). These are low-current welds (50–80 A) with comparatively low-electromagnetic (Lorenz) forces, easily influenced by Marangoni flow.

Marangoni-driven fluid flow is associated with a gradient in the surface tension affected by a dependence upon temperature. Flow is always away from regions of low surface tension to regions of high surface tension. For most aluminum alloys, the slope of the surface tension vs. temperature is negative ( $d\gamma/dT < 0$ ), which means that the center of the weld pool (hottest region) will have the lowest surface tension and flow will be outward. Subsurface convection cells may be formed, influenced by these surface flow patterns.

There have been only a limited number of studies modeling fluid flow patterns within aluminum weld pools. Kou and Sun (Ref. 23) made predictions for fluid flow in an Aluminum Alloy 6061 weld, assuming a current of 150 A and a negative surface tension temperature coefficient ( $d\gamma/dT = -0.35 \text{ mN}/(\text{m}\cdot\text{K})$ ), that surface tension would overpower electromagnetic and buoyancy forces, resulting in an outward flow at the surface. In comparison to ferrous alloys, this would be analogous to welding a low-sulfur stainless steel.

For the case of Aluminum Alloy 1100, the surface tension temperature coefficient for commercial pure aluminum has been measured in argon to be  $-0.15 \text{ mN}/(\text{m}\cdot\text{K})$  (Ref. 24). This is less than half of the  $-0.35 \text{ mN}/(\text{m}\cdot\text{K})$  value used by Kou and Wang (Ref. 22) for Alloy 6061. This lower  $d\gamma/dT$  slope may explain the reversed flow observed in this study, where the weaker outward contribution from Marangoni flow became overpowered by the inward electromagnetic-driven flow.

Hypothetical calculations by Kou and Wang (Ref. 22) have demonstrated that smaller or positive values of surface tension temperature coefficient can reverse flow direction from outward to inward at the weld pool surface. In this same paper, the authors postulated that outward flow at the surface would

interfere with pore escape, resulting in more pores becoming entrapped. Although this study did not analyze this effect directly, this could explain how the macropores that formed near the surface of the leading edge of the weld pool were able to grow in Alloy 6061. It is not well understood or documented for aluminum alloys how alloying elements affect the surface tension temperature coefficient. In one source (Ref. 25), magnesium was found to lower surface tension even when present in small amounts.

## Pore Growth

All macropores grew over time before being engulfed or ejected from the weld pool. The very largest pores could not be engulfed and were ejected. In only a few instances were pores observed to coalesce, as shown in Fig. 11. It follows that growth was achieved primarily through diffusion of hydrogen from the liquid to the pore. Higher hydrogen supersaturation in the liquid should then result in faster growth, as predicted by Fick's Law. While the hydrogen concentration along the solid/liquid boundary is likely higher than in the bulk, due to partitioning during solidification, there is nonetheless a relation between bulk hydrogen and growth rate, as depicted in Fig. 12. These measurements could only be made for Alloy 6061 welds, which consistently had spherical-shaped pores. It was found that the highest hydrogen additions gave the fastest growth rate.

## Conclusions

These conclusions are based upon edge-weld observations, which may or may not apply directly to more-common weld geometries.

1) Results from in-situ radiography during aluminum GTAW substantiated an earlier proposed hypothesis that macropores

form when hot, supercharged liquid under the arc moves to the cooler pool periphery.

2) The initial location and migration pattern of macropores was shown to vary with alloy content. Alloy 4047 was unique in that it had almost no macropores, whereas Alloy 1100 had the most macropores (elongated) located near the weld pool bottom, and Alloy 6061 had the most macropores (spherical) located near the weld pool top.

3) Alloy 1100 macropores originated at the bottom of the weld pool and then migrated upward toward the rear of the pool. Macropores in Alloys 4047 and 6061 originated at the leading edge of the weld pool and then moved downward and toward the rear of the pool. Differences in behavior between Alloy 1100 and Alloys 4047 and 6061 are believed to be related to different fluid flow patterns affected by electromagnetic and Marangoni forces.

4) Pore growth was achieved primarily through the diffusion of hydrogen from the liquid to the pore. Macropore volume and growth rate increased with an increasing amount of hydrogen in the shielding gas.

5) The limited resolution of the used radiographic equipment did not allow detailed evaluation of micropore evolution. The smallest pore that could be measured was about 90  $\mu\text{m}$ .

## Acknowledgments

This work was supported by the U.S. Department of Energy through the Los Alamos National Laboratory. Los Alamos National Laboratory is operated by Triad National Security LLC for the National Nuclear Security Administration of the U.S. Department of Energy (contract no. 89233218CNA000001). Special thanks to Mike Steinzig for funding support; J.D. Montalvo and Jessica Lopez for metallographic support; Tim Baker for gravimetric measurement support; Chris Stull, Amber DeLaO, Timothy Ickes, and Kelley Vansyoc for radiographic technical support; and Jesse Martinez for insight and welding support.

## References

1. Talbot, D. E. J. 2004. *The Effects of Hydrogen in Aluminum and Its Alloys*. London: Maney Publishing.
2. Honig, E. M. 1974. Effects of cluster porosity on the tensile properties of butt weldments in T-1 steel. Army Construction Engineering Research Laboratory, Champaign, Ill.
3. Andrew, R. C. 1975. Sources of hydrogen porosity in aluminum alloy welds. *Australian Welding Research* 4(2): 1–19.
4. Opie, W. R., and Grant, N. J. 1950. Hydrogen solubility in aluminum and some aluminum alloys. *Transactions AIME* 188: 1237–1241. DOI: 10.1007/BF03399138
5. Zacharia, T., Eraslan, A. H., and Aidun, D. K. 1988. Modeling of autogenous welding. *Welding Journal* 67(3): 53-s to 62-s.
6. Woods, R. A. 1974. Porosity and hydrogen absorption in aluminum welds. *Welding Journal* 53(3): 97-s to 108-s.
7. Gedeon, S. A., and Eagar, T. W. 1989. Thermochemical analysis of hydrogen absorption in welding. *Welding Journal* 69(7): 264-s to 271-s.
8. Cross, C. E., Olson, D. L., and Liu, S. 2003. "Chapter 9: Aluminum welding." *Handbook of Aluminum: Physical Metallurgy and Processes*, 481–532. CRC Press LLC. DOI: 10.1201/9780203912591
9. Coniglio, N., and Cross, C. E. 2009. Mechanism for solidification crack initiation and growth in aluminum welding. *The Minerals,*

*Metals & Materials Society* 40A: 2718–2728. DOI:10.1007/s11661-009-9964-4

10. Campbell, J. 1991. *Castings*. Oxford, Great Britain: Butterworth-Heinemann.

11. Farzadi, A., Serajzadeh, S., and Kokabi, A. H. 2010. Investigation of weld pool in aluminum alloys: Geometry and solidification microstructure. *International Journal of Thermal Sciences* 49(5): 809–819. DOI: 10.1016/j.ijthermalsci.2009.11.007

12. Stefanescu, D. M., Juretzko, F. R., Dhindaw, B. K., Catalina, A., Sen, S., and Curreri, P. A. 1998. Particle engulfment and pushing by solidifying interfaces: Part II. Microgravity experiments and theoretical analysis. *Metallurgical and Materials Transactions A* 29: 1697–1706. DOI: 10.1007/s11661-998-0092-3

13. Dixon, B., Baldwin, N., and Coghill, M. 1988. Real time radiography of weld solidification. *Australian Welding Research* 16(12): 70–74.

14. Rokhlin, S. I., and Guu, A. C. 1990. Computerized radiographic sensing and control of an arc welding process. *Welding Journal* 69(3): 83-s to 97-s.

15. Fujinaga, S., Takenaka, H., Narikiyo, T., Katayama, S., and Matsunawa, A. 2000. Direct observation of keyhole behaviour during pulse modulated high-power Nd:YAG laser irradiation. *Journal of Applied Physics D: Applied Physics* 33: 492–497. DOI: DOI:10.1088/0022-3727/33/5/304

16. Katayama, S., Kobayashi, Y., Mizutani, M., and Matsunawa, A. 2001. Effect of vacuum on penetration and defects in laser welding. *Journal of Laser Applications* 13: 187–192. DOI: 10.2351/1.1404413

17. Boateng, F. T., Ewert, U., Kannengiesser, T., Griesche, A., Zscherpel, U., Kromm, A., Hohendorf, S., and Redmer, B. 2016. Real-time radiography for observation of crack growth during GTA welding. *Welding in the World* 60: 931–937.

18. The Aluminum Association. 1984. *Aluminum Standards and Data*, 38–39.

19. Sekulic, D. 2018. Brazing of aluminum alloys. *ASM Handbook, Volume 2A, Aluminum Science and Technology*, 763–782. Materials Park, Ohio: ASM International. DOI: 10.31399/asm.hb.v02a.9781627082075

20. Suban, M., and Tusek, J. 1998. Influence of hydrogen in argon as a shielding gas in arc welding of high-alloy stainless steel. *Annual Assembly of the International Institute of Welding*, Hamburg, Germany.

21. Barraza, A. M. 2021. In-situ radiography of hydrogen porosity growth and development in aluminum welds. Master's thesis, The Ohio State University, Los Alamos National Laboratory, Los Alamos, N.Mex.

22. Kou, S., and Wang, Y. 1986. Weld pool convection and its effect. *Welding Journal* 65(3): 63-s to 70-s.

23. Kou, S., and Sun, D. K. 1985. Fluid flow and weld penetration in stationary arc welds. *Metallurgical Transactions A* 16A: 203–213. DOI: 10.1007/BF02815302

24. Saravanan, R. A., Molina, J. M., Narciso, J., Garcia-Cordovilla, C., and Louis, E. 2002. Surface tension of pure aluminum in argon/hydrogen and nitrogen/hydrogen atmospheres at high temperatures. *Journal of Material Science Letters* 21(4) 309–311. DOI: 10.1023/A:1017988223416

25. Bainbridge, I. F., and Taylor, J. A. 2013. The surface tension of pure aluminum and aluminum alloys. *Metallurgical and Materials Transactions A* 44(8): 3901–3909. DOI:10.1007/s11661-013-1696-9

**ALEXIYA M. BARRAZA, CARL EDWARD CROSS, CHRISTOPHER JASON STULL, and JESSE N. MARTINEZ** are with TRIAD LLC, Los Alamos National Laboratory, Los Alamos, N.Mex. **CAROLIN FINK** (*fink.242@osu.edu*) is with the Department of Materials Science and Engineering, The Ohio State University, Columbus, Ohio.